Article

Contribution of High-Resolution Digital Twins for the Definition of Rockfall Activity and Associated Hazard Modelling

Carlo Robiati[1], Giandomenico Mastrantoni[2,*], Mirko Francioni[1,3], Matt Eyre[1], John Coggan[1] and Paolo Mazzanti [2,4]

[1] Camborne School of Mines, University of Exeter, Penryn, Cornwall TR10 9EZ, UK
[2] Department of Earth Sciences & CERI Research Centre, Sapienza University of Rome, Piazzale Aldo Moro 5, 00185 Rome, Italy
[3] Department of Pure and Applied Sciences, Carlo Bo University of Urbino, Urbino, Marche, Italy
[4] NHAZCA S.r.l., Via Vittorio Bachelet 12, 00185 Rome, Italy
* Correspondence: giandomenico.mastrantoni@uniroma1.it.

Abstract: The increased accessibility of drone technology and the wide use of Structure from Motion 3D scene reconstruction have transformed the approach for mapping inaccessible slopes undergoing active rockfalls. The Poggio Baldi landslide offers the possibility for many of these techniques to be deployed and integrated with the aim of defining a suitable workflow for the analysis of hazards in mountainous regions. The generation of multitemporal digital slope twins (2016 – 2019), informed a rockfall trajectory analysis that was carried out with a physical-based GIS model. We tested the rockfall scenario reconstructed and calibrated on the analysis of the rock mass characteristics and the geometrical and physical constraints given by the multi-temporal analysis of the SfM point clouds. This time-independent rockfall hazard analysis is a critical component to any subsequent holistic risk analysis on this case study, and any potential similar mountainous setting.

Keywords: Rockfall Hazard; Remote Sensing; 3D Modelling.

1. Introduction

Rockfall hazard is a well-known mass wasting phenomenon in mountainous regions. Notably, a rockfall has unusual properties, such as extreme velocity and its catastrophic nature, posing a very complex condition to act against. Due to this, in the last year, new software and techniques for the study and simulation of this phenomenon have been developed. Some examples are represented by [1] and [2], which showed the use of UAV and GIS-based codes for runout simulations in the Central Apennines of Italy and East Spain, respectively. [3] developed a new method to extract vegetation during simulation while [4] highlighted identification of rockfall source areas at the regional scale through probabilistic analyses.

During a rockfall event, potential damages are associated with rocks reaching vulnerable elements during their descent down the slope [5–7]. The volumes involved in a rockfall, its velocity and trajectories are the parameters that are directly related to the severity of the consequences of the event. The trajectories of the rock fragments depend on the slope geometry and the characteristics of the propagation zone, local asperities (i.e., jump features) and the mechanical characteristics of the exposed bedrock and soil cover. The quality of the results of rockfall analysis/simulations is directly related to the input parameters used. In particular, the geometry of the propagation area, the volume of the potential failing blocks and the coefficient of restitution are key parameters during the simulations [8]. The geometry of the propagation area and coefficient of restitution can be interpreted using remote sensing data and field observations [9,10], while the volume of blocks can be defined using geomechanical data or through the analysis and interrogation of past failures when available [11,12]. In this context, one of the problems that often arise

 doi:10.20944/preprints202212.0142.v1

in rockfall simulations is the definition of rock block volume when the structural condition, and consequently rock block volumes, vary within the slope [1,13]. In this study, we present a new approach to overcome such a problem. A multitemporal remote sensing analysis of the slope has been carried out to highlight different rockfall source sectors within the study area. In these sectors, we have surveyed the discontinuity sets and their characteristics, such as spacing and persistence. These data were then used to calculate the volume of potential rock blocks characterizing each area. Through this approach, it was possible to perform detailed rockfall simulations for each source area using specific structural/geomechanical data. The case example used for this purpose is the Poggio Baldi (PB) landslide, in the Italian northern Apennines.

2. Study Area

The Poggio Baldi landslide (Figure 1) is in the Appennino Forlivese (Northern Apennines), in the vicinity of Poggio Baldi village. Poggio Baldi falls within the Foreste Casentinesi National Park in the Santa Sofia municipality (Forlì-Cesena FC, Emilia-Romagna). The landslide spans across 845 m asl with its main scarp, to 467 m asl, where the Bidente river cuts across the landslide body's toe, and the road SS310 runs parallel to it. The Appennino Forlivese belongs to the Tosco-Emiliano sector of the Northern Apennines, a trust and fold orogenic belt, verging N-E and oriented WNW-ESE approximately [14]. The Bidente river valley cuts into the Marnoso-Arenacea Formation (FMA), Miocenic age [15], and it is involved in a series of NW-SE oriented thrusts. The thrust front is cut by a series of high-angle direct faults, nearly orthogonal to it. The FMA is composed of an alternate of sandstones and mudstones [16,17], showing well-defined and regular Bouma sequences, described in [18]. The geomorphological setting is strongly controlled by the FMA lithologies combined with the geo-structural evolution of the region. Along the Bidente river valley, the slopes geometry is influenced by the juxtaposition of marls and sandstones. In the thrust back limb, strata are organized approximately in a monoclinal, gentle dipping structure (circa 30°) perpendicular to the main NW-SE thrust [19].

The PB landslide is one of the largest slope instabilities of this Apennine sector, it is estimated it has mobilized close to $4x10^6$ m^3 of rock, and it is considered to still be active, with a reactivation frequency of 100 years. Its main catastrophic events occurred in March 1914 and March 2010. The landslide's initial activation is considered a large-scale wedge failure mechanism, inferred by the scarp geometry [20]. The latest reactivation occurred between March 18 and 19, 2010, when approximately 4 million cubic meters of material were mobilized, creating severe damages to several buildings and to the road SS310 [21,22]. After the development of tension cracks the landslide body began to slowly move downward, reaching the Bidente river in 3 hours, engulfing circa $16x10^4$ m^2, and damming the river, creating an ephemeral lake extending for $35x10^3$ m^2. The pluviometric archives report an unusual amount of rain and snow in the winter season before the reactivation; for this reason, it is considered to be one of the main triggers, as well as the continuous ravelling of material from the summit of the scarp. The overload caused by the fallen blocks could have played a role in destabilizing the landslide body; some research estimated the increase of material resting below the main scarp of 40 m [21].

According to [23], this landslide can be classified as complex, a roto-translational slide evolved into an earthflow, with rockfall associated with the upper portion of the sub-vertical rock wall. The main scarp extends linearly for about 300 m, and its sub-vertical rock wall measures more than 100 m (Figure 2), with many suspended water conduits that seep through the rock mass and emerge within the rock wall. This is a highly unstable condition leading to continuous rock falls that has led to the deployment of several protection structures, three sand berms positioned at the toe of the debris body. In this study, we focus on the rockfall hazard, posed by the continuous ravelling of rock blocks and its potential impact on human activities in the area affected by the rock falls.

In October 2021, the Poggio Baldi landslide became a permanent natural monitoring laboratory managed by the Department of Earth Sciences of Sapienza University of Rome.

Preprints (www.preprints.org) | NOT PEER-REVIEWED | Posted: 8 December 2022 doi:10.20944/preprints202212.0142.v1

The lab employs the most advanced remote sensing tools to monitor the activity of the main rock scarp and the related debris talus at its toe. Over the years, many surveys and investigations have been carried out using modern remote sensing techniques (e.g., Terrestrial Laser Scanner, Drone Photogrammetry, Terrestrial-InSAR, Gigapixel imaging, and PhotoMonitoring™) in order to acquire as much information as possible about active gravitational processes [22,24,25].

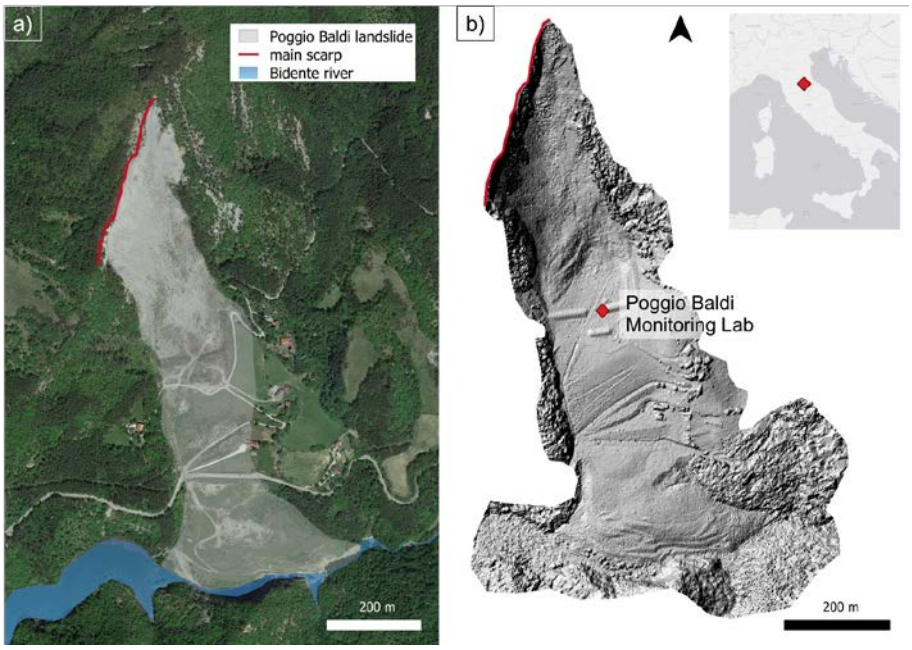

Figure 1. Poggio Baldi landslide overview. The main, sub-vertical landslide scar is highlighted in red (a); The location of the Poggio Baldi Monitoring Lab is also reported in the DEM (b).

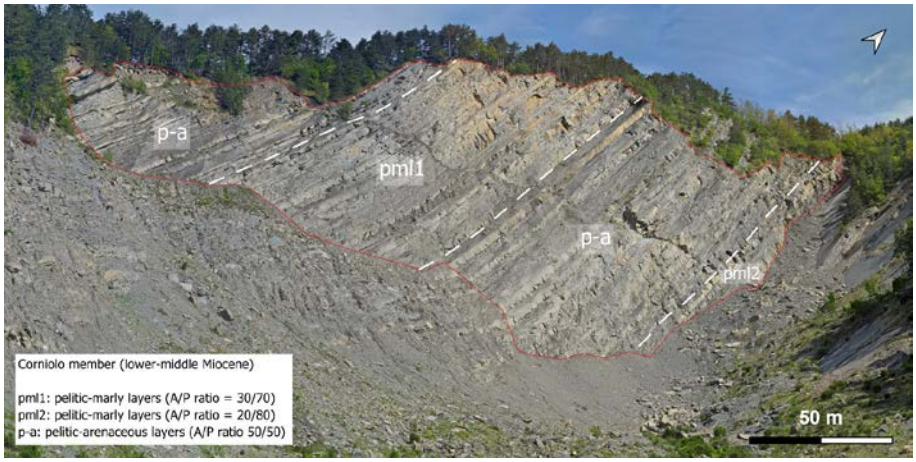

Figure 2. Front view of the Poggio Baldi landslide main scarp. The three different members of the Marnoso-Arenacea Formation are distinguished by the different content ratios of marly and arenaceous strata.

3. Material and Methods

This paper aims to present a new method to study the potential rockfall trajectories based on the identification of different source areas, through use of multitemporal remote sensing data, and detailed structural analysis. Drone-based digital photogrammetry (DP), with Structure from Motion (SfM) techniques, have been exploited for the creation of slope digital twins. The geostructural characteristics of both the slope and the rock mass were extracted from both the generated point cloud and orthomosaic, these were successively used to compute mean spacings and rock block volumes. Rock-mass characterization and

 doi:10.20944/preprints202212.0142.v1

the rock block volumes were identified for each source sector to simulate the trajectories of falling blocks and define hazard zones. The results gathered by the presented approach were validated against past rockfall events recorded by different instruments during the years.

3.1. Digital Twin Models

This section will present the digital twin models that have been built and exploited to detect rockfall and accumulation areas and to derive the geostructural model. Digital Photogrammetry (DP) from multitemporal drone surveys was implemented to derive three-dimensional point clouds and a high-resolution orthomosaic of the main rock scarp. The resulting point clouds were managed and processed within the software Cloud Compare [26]. The integration of information obtained from point clouds and the orthomosaic serves the purpose of obtaining a reliable geostructural dataset (i.e., the discontinuity sets, their spacing, and the distribution of in-situ rock blocks). Multitemporal surveys allowed us to identify and quantify rockfalls and subsequent debris accumulation.

Structure from Motion (SfM) is a technique capable of reconstructing a high-resolution 3D digital twin of object under investigation. It was developed during the nineties [27–29], based on the same stereoscopic principles of digital photogrammetry (DP), whereas the computer vision scientific community implemented most of the algorithms we use nowadays [30–32]. The SfM technique exploits the detection of homologous key points over large photographic datasets, obtained with a large amount of redundancy and partial overlap among the pictures. That enables the reconstruction of a sparse and a dense point cloud, and finally the 3D object [33]. This technique has made the use of DP easier and more attractive. In this study, a DJI Phantom 4 drone equipped with GPS, an IMU apparatus, and a 12.4 MPx onboard camera with a 1/2.32-inch sensor size and a 20 mm lens has been used for the survey of the study area. The drone flights were made between 1:00 PM and 3:30 PM CET in April 2016 and May 2019. A total of 950 photographs were collected from different lines of sight, maintaining a constant distance from the outcrop. An overlap of about 70-80% was preserved between the frames. Both the reconstructed point clouds were georeferenced in the WGS84 UTM 32T coordinate system using a GNSS survey conducted during the landslide survey. Two dense point clouds (shown in Figure 3) were generated by means of the Structure from Motion (SfM) workflow implemented in the Agisoft LLC Metashape software [27–29,33–36].

The photogrammetric point clouds (PC) have a total of 26.6 x 10^6 and 73 x 10^6 points respectively. The actual resolution was established after cropping the rocky scarp, which is 220 pt/m^2 and 657 pt/m^2 for the 2016 and 2019 PC respectively. A preprocessing stage was carried out to standardise the PC and make them comparable (i.e., minimum distance between nearest points at 0.1 m). The PC were analysed and compared via Cloud-Comapre® v.2.10.2 [26]. The pair of multitemporal point clouds was compared by taking advantage of the M3C2 algorithm [37], taking care of accounting for the registration error which RMSE is equal to 0.2 meters. This algorithm does not require interpolation but estimates the normals to the surfaces and distances directly from the point clouds [37,38]. The three-dimensional comparison enabled us to identify specific sectors of the Poggio Baldi landslide reporting significant changes caused by rockfalls or deposition phenomena. In addition to the geometric localisation of these sectors, volume changes were measured with the 2.5D volume calculation algorithm embedded in CloudCompare® v. 2.10.2, which relies on the rasterization of clouds.

Preprints (www.preprints.org) | NOT PEER-REVIEWED | Posted: 8 December 2022 doi:10.20944/preprints202212.0142.v1

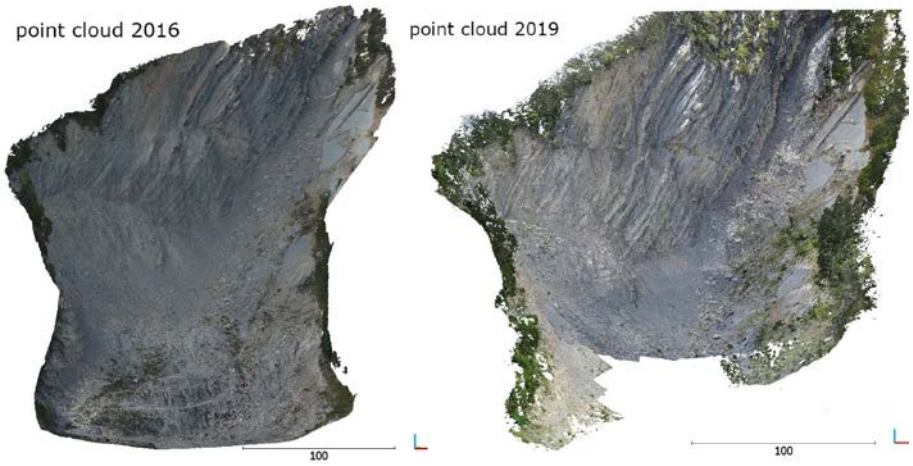

Figure 3. SfM-based point clouds derived from the drone photogrammetric survey. Two campaigns were carried out in April 2016 (left) and May 2019 (right).

Following the point cloud reconstruction, an orthomosaic image of the rock scarp was computed from a set of overlapping drone images with the corresponding referencing information (Figure 4). It was derived from a process where several overlapping photos are stitched together with distortions removed to create a complete and continuous image representation of the rock scarp. An algorithm known as orthorectification is used to modify the photos based on the DSM information so that features are in their true location. Finally, the orthorectified images are merged into a single orthomosaic which were used to accurately measure distances and to investigate fracture patterns.

The Poggio Baldi orthomosaic is derived from the drone images acquired during the May 2019 survey. After having constructed the point cloud and the related DSM, a bounding box delimiting the rock scarp was defined prior to performing the orthorectification process. The final product covers a total area of about $40x10^3$ m^2 with a pixel size of 2.1 cm.

Figure 4. Orthomosaic extracted from the 2019 UAV survey.

3.2. Slope Analysis

This section describes the remote sensing-based approach that has been used to characterize the rock-mass geostructural properties.

With the goal of extracting the main discontinuity features we have utilized the 3D discontinuity set extractor tool. As described in [39,40], the Discontinuity Set Extractor (DSE), is a MATLAB™-based algorithm designed to extract the discontinuity's geometrical properties from a laser or photogrammetric point cloud. The distinctive feature of DSE is to exploit the real 3D information contained in each point and its corresponding neighbours to identify local differences in the geometry of the slope with no need to generate a mesh. The algorithm considers the points within a neighbouring space to compute best-fitting planes and attribute values directly to each point, rather than the fitting

 doi:10.20944/preprints202212.0142.v1

patches. By using the raw data, the spatial orientation of each point is calculated only if it is coplanar with the adjacent points. This allows relative measurements to be obtained for each point rather than a single measurement for each surface identified in a 2.5D mesh. When the slope surface is primarily defined by discontinuity faces, the points in the cloud can be appropriately grouped into sets that define the predominant orientations and thus the discontinuity systems. Therefore, the joint sets are extracted in three main steps: i) local curvature computation by means of knn-search [41] and PCA algorithm; ii) statical analysis using the 2D Kernel Density Estimation function (kde2d) [42] in order to define the main joint sets; iii) cluster analysis through the DBSCAN algorithm [43] which allows establishing points close enough to be considered as a single surface.

Since point clouds are intrinsically non-uniform in terms of point density, a subsampling process was required. The selected minimum spatial distance between two adjacent points was set to 0.1 meters. Therefore, this pre-processing step allowed uniform point densities throughout the rock scarp, thus reducing the problem of under- and over-represented surfaces (i.e., fewer points per area and more points per area respectively) that would have biased the discontinuity extraction process. The discontinuity extraction was performed on the 2019 rock scarp point cloud following the modified approach implemented by [44]. Dominant densities were identified and removed together with debris accumulations along the slope. Removal of the dominant joint set allowed the identification of the least represented surfaces. The value of the knn parameter was set equal to the mode of the k-nearest neighbours within an area of $1m^2$. This value reflects the scale of the investigation and the need to overcome the complex local geological conditions (i.e., sandstone and marl-clays alternations) which determine strong variations in the roughness of the exposed surfaces. Once the joint sets were extracted, the 3D normal spacing of each joint set was computed by analysing the relative position of each joint (considered as non-persistent) and measuring the orthogonal distance between them [45]. The mean normal spacing values were then exploited to compute the mean block volumes at each selected sector of interest [46]. Discontinuity systems that are only kinematically compatible to any type of failure were considered to be factors constraining the block volumes.

In addition to the three-dimensional analysis carried out by DSE, the orthomosaic has been exploited by manually tracing the discontinuity planes at four selected representative areas of 400 m^2 (20x20m square) along the rock scarp. The vectorized fracture traces were subsequently analysed with the FracPaQ toolbox [47] in order to quantify fracture patterns and spacings. FracPaQ is an open-source, cross-platform, toolbox with a collection of MATLAB™ programs designed to quantify fracture patterns in two dimensions from digital data with user control over the output. Quantitative estimates for the attributes of individual fractures are returned as outputs. Since FracPaQ assumes that the input traces lie on a statistically flat surface, the investigated areas were adequately chosen within the source zones. Finally, to better constrain the bedding geometrical features, manual measurements on the orthomosaic were carried out. As a result bedding spacings were integrated with the information derived from the 3D point cloud, thus constricting the mean block volumes.

3.2.1 Rockfall hazard analysis and numerical modelling

From the different methods available to assess susceptibility and hazard for rockfall events [48–50], and characterise the 3D rockfall events [51], we selected a well-established strategy to quantify the probability for a rock fall to reach vulnerable elements and generate negative consequences. Probabilistic rockfall trajectory analysis tries to minimise both ontic and epistemic uncertainty by introducing a certain degree of variability in the inputs [52]. As described by [53], the geometry of the slope plays a critical role in guiding the rockfall path down the slope, a digital elevation model of this geometry is the fundamental dataset that numerical simulations rely upon. Defining the characteristics in terms of elasticity of the slope is of critical importance [54,55] as well and, to achieve this, the slope is divided in homogeneous areas exhibiting similar mechanical characteristics. The

 doi:10.20944/preprints202212.0142.v1

rockfall model was implemented using Rockyfor3D, and the outcomes of the simulation runs were post-processed in GIS to be further investigated. The physical characteristics of the slope were assigned through digital mapping of the slope domains, such as scree average diameter, outcropping bedrock, and thickness of the debris cover; the mapping was validated through both photointerpretation of the high-resolution images from the drone survey and the field observations. The values in terms of R_n were assigned following the guidelines given by [52,56], the MOH values were modified according to the expert judgement and the availability of direct measurement of the scree geometry on the point cloud (2019).

Fundamental information needed to generate accurate rockfall models is the topographical representation of the slope. In the case of GIS-based methods, DEM provides the virtual surface from which to compute the types of motion (freefall, bounce, roll or drag) of the falling rock blocks.

This paper used 3-dimensional process-based physical simulation to describe the potential trajectories of the released rock and their endpoints, the energy dissipated along the runout and the bounce height. For this analysis we have used the GIS-based Rockyfor3D software. This is a spatially distributed, probabilistic, processed-based code for rock fall trajectory analysis. It exports a series of ascii rasters which are used to generate input parameters in the numerical modelling. I.e., it uses a digital elevation model of the slope to assign mechanical characteristics needed for the computation of velocity and energies before and after impacts.

Fundamental information needed to generate accurate rockfall models is the topographical representation of the slope. In the case of GIS-based methods, DEM provides the virtual surface from which to compute the types of motion (freefall, bounce, roll or drag) of the falling rock blocks.

Rockyfor3D uses a three-dimensional rigid-body impact model that allows the calculation of trajectories of single, individually falling rocks with discrete geometry. This software can be used for regional, local and slope-scale rockfall simulations [56]. The input parameters that define rock blocks are the release cell location, the rock density, the shape and volume and initial vertical velocity. The local slope surface roughness is represented by a parameter defined as height of a representative obstacle (MOH), expressed in m. Typical MOH values, as suggested by [56], are represented by three statistical classes, rg70%, rg20%, and rg10%. During each rebound calculation, the MOH value in a cell is randomly chosen from the three representative values according to their probabilities of occurrence. Finally, the soil type is defined through a raster map identifying the type of bedrock exposed.

$$R_t = \frac{1}{1 + ((MOH + D_p)/R)} \quad (1)$$

Where MOH (Mean obstacle height) or r_g values are estimated, D_p is the penetration depth of the block and R is the radius of the computed block, in RF3D the maximum penetration depth equals the radius of the falling block. In this study, we used a 3 × 3 m resolution DEM extracted from the 2019 SfM point cloud. The locations of release points were selected based on 3D change detection. Field inspection and geomorphological analysis of high-resolution aerial images were undertaken to define Slope roughness (MOH values) and soil type (R_n). The tangential coefficient of restitution (R_t) is automatically calculated by Rockyfor3D through the composition and size of the material covering the surface and the radius of the falling block [56]. The rock density, shape, and volume were defined by combining field and remote sensed geostructural data. For modelling the upper scarp's rockfalls in Poggio Baldi we relied on a variety of remote sensing techniques, each contributing to constrain the numerical modelling. The position of the source and deposition areas was extracted from the M3C2 analysis. The modelled scenarios were defined a priori based on the slope geomechanical analysis and the distribution of rockfall fragments along the slope. The M3C2 change detection was critical to select the objective source areas on the slope; the volumetric classes were chosen as the most representative for the analysis

Preprints (www.preprints.org) | NOT PEER-REVIEWED | Posted: 8 December 2022 doi:10.20944/preprints202212.0142.v1

to be carried out. Although we consider this analysis to be time independent there are some considerations about the magnitude of the rockfall simulated.

4. Results

In this section the results obtained from the SfM-based point cloud, as well as from the orthomosaic processing, are presented with respect to three-dimensional changes and rock mass characterization. Furthermore, block volume estimations are exploited as input to model the rockfall-associated hazard.

4.1 3D Change Detection

The 3D change detection led us to identify geometrical differences representative of three years of gravitational processes along the study area. Sectors in which there is a negative difference correspond to loss areas, (i.e., highly unstable areas subject to rockfall). In contrast, areas in which there is a positive difference correspond to accumulation areas, which are located along the base of the scarp consisting of heterogeneous debris accumulated over time (Figure 5). Results reveal how four portions of the scarp are more affected by rockfalls. Hereafter, we refer to these most active sectors in terms of rock block release with Z1, Z2, Z3, and Z4 as reported by the white dashed polygons in Figure 5. Over the time span being considered, the four source zones discharged more than 3000 m^3 of rock materials which accumulated in the debris talus at its toe, as revealed by the 3D change detection (Table 1).

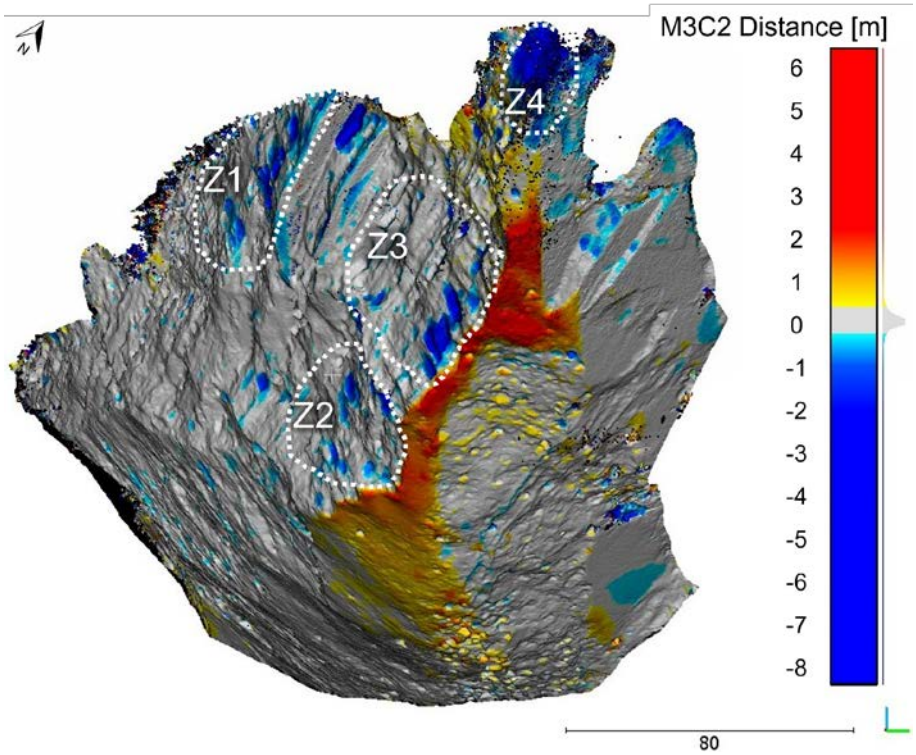

Figure 5. Analysis of three-dimensional differences between the 2016 and 2019 SfM-point clouds. White contour lines indicate sectors from which the largest volumes of rock have detached. The colour bar is saturated at ± 8m, and the detection threshold is set to ± 0.3m.

Table 1. Surface and volume estimation related to rockfall processes occurred between Aprile 2016 and May 2019 at the Poggio Baldi rock scarp.

Source Sector	Process	Estimated Surface [m^2]	Estimated Volume [m^3]
1	Rockfalls	1441	620
2	Rockfalls	1805	475
3	Rockfalls	2795	817

Preprints (www.preprints.org) | NOT PEER-REVIEWED | Posted: 8 December 2022 doi:10.20944/preprints202212.0142.v1

4	Rockfalls	1479	1196
Toe	Debris accumulation	4572	5160

4.2 Geostructural Characterization

The 3D geo-structural analysis carried out on clipped point clouds representative of the four source zones led us to group the exposed fracture planes into five different joint sets (Figure 6). Although within each of the individual zones along the scarp it is clear that there are five dominant discontinuity sets, some differences are observed concerning their principal orientation (Figure 7). Similarity appears to be between Z1 and Z2 as well as between Z3 and Z4. Among the source zones, the J3, which represents the north-dipping discontinuities, appears to be the joint set varying the most, whereas the J1 (i.e., slope face) results to be the most dominant and conform set (Table 2). Bedding strata grouped as J2, are south dipping with a dip angle varying from 33 to 46 degrees.

Joint spacings were estimated for each discontinuity set and each analysed sector. The distribution of measured spacing values is depicted on the density plots (Figure 8) for each slope sector assuming non-persistent joints. Based on spacing densities, J1, J4, and J5 have evenly distributed spacing values along the sectors, resulting in skewed peak densities around 1.5 meters. J2 and J3, which are represented by a minor number of discontinuities planes with roughly distributed spacing values, result in wide density distribution characterised by long tails and no tight peak. Following the distribution analysis, it is clear that the mean spacing of J2 derived from the 3D PC does not represent an accurate value, thus leading to the need to better constrain the bedding strata. Mean spacing values related to density curves are summarised in Table 3.

In fact, the bedding strata J2 are highly underestimated by the DSE analysis due to their orientation (orthogonal to the slope face) and the low presence of daylighting surface to be measured, thus affecting the three-dimensional geo-structural results and all the related analysis (e.g., joint spacings). To overcome this limitation, the discontinuity planes were also mapped in the orthomosaic within square boxes of 20m per side (Figure 9). As a result, scalable vector graphics with discontinuity traces composed of one or more segments delimited by nodes were obtained thus allowing the computation of quantitative patterns with a focus on the bedding strata (Figure 10).

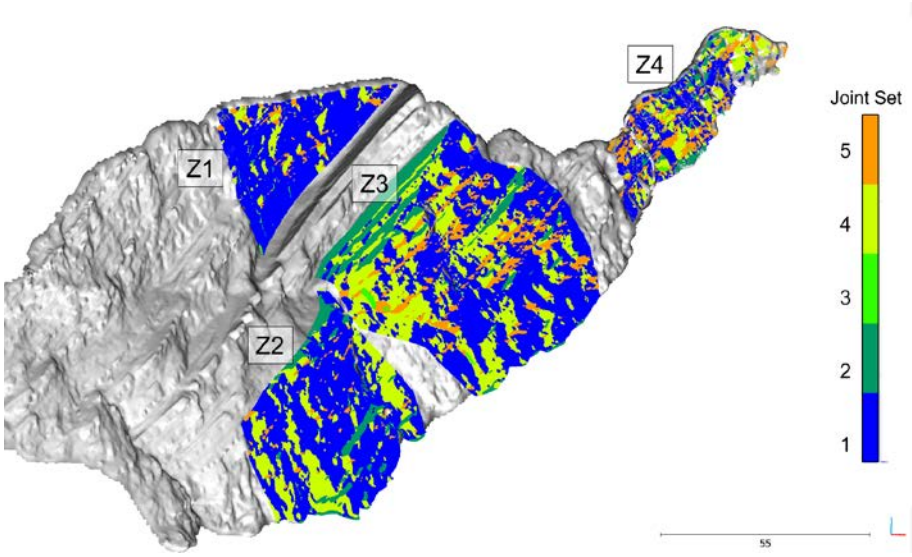

Figure 6. Poggio Baldi rock scarp with discontinuity planes within each source sector coloured according to the assigned joint set.

Preprints (www.preprints.org) | NOT PEER-REVIEWED | Posted: 8 December 2022 doi:10.20944/preprints202212.0142.v1

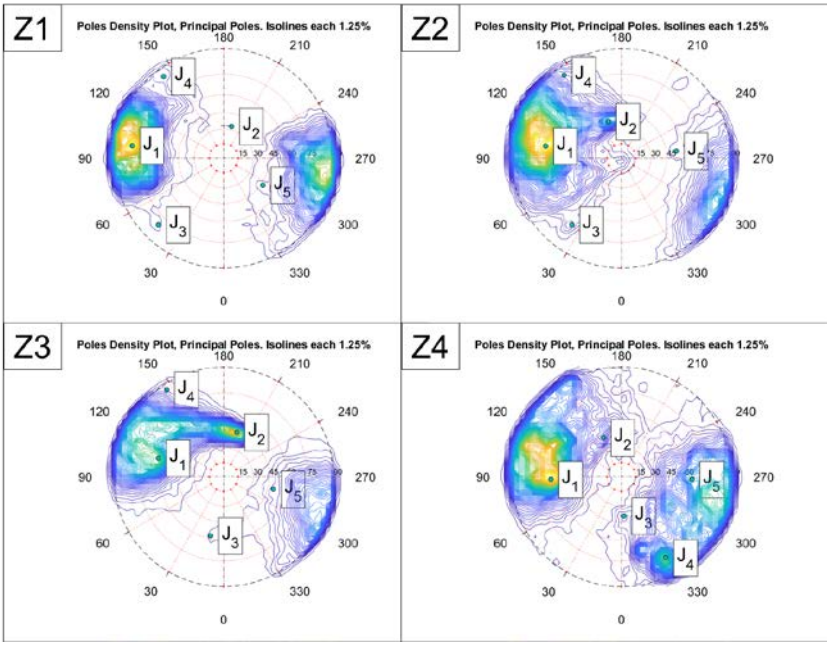

Figure 7. Stereoplot of discontinuity planes extracted by means of DSE software at the selected source sectors.

Table 2. Principal orientations of discontinuities extracted from source sectors of the 2019 SfM point cloud.

Joint Set	Type of Discontinuity	Z1		Z2		Z3		Z4	
		Dip-Dir	Dip-Angle	Dip-Dir	Dip-Angle	Dip-Dir	Dip-Angle	Dip-Dir	Dip-Angle
1	Slope Face	98	80	99	70	105	64	88	65
2	Bedding	194	33	160	39	196	46	155	43
3	Minor Joint	44	80	37	74	12	57	356	39
4	Minor Joint	143	85	145	85	146	87	331	80
5	Minor Joint	304	47	262	54	284	50	272	65

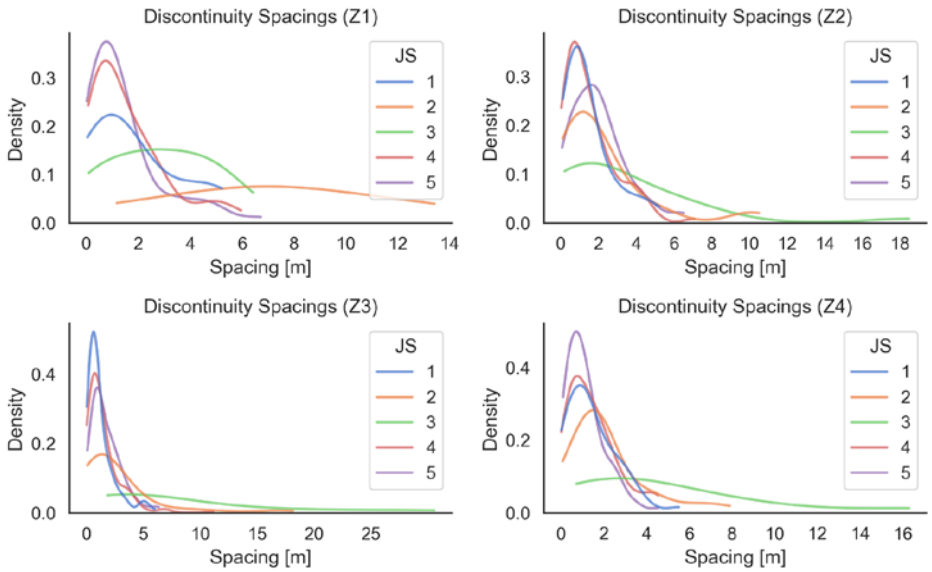

Figure 8. Normal spacing values distribution of discontinuity planes by joint set and source zone.

Preprints (www.preprints.org) | NOT PEER-REVIEWED | Posted: 8 December 2022 doi:10.20944/preprints202212.0142.v1

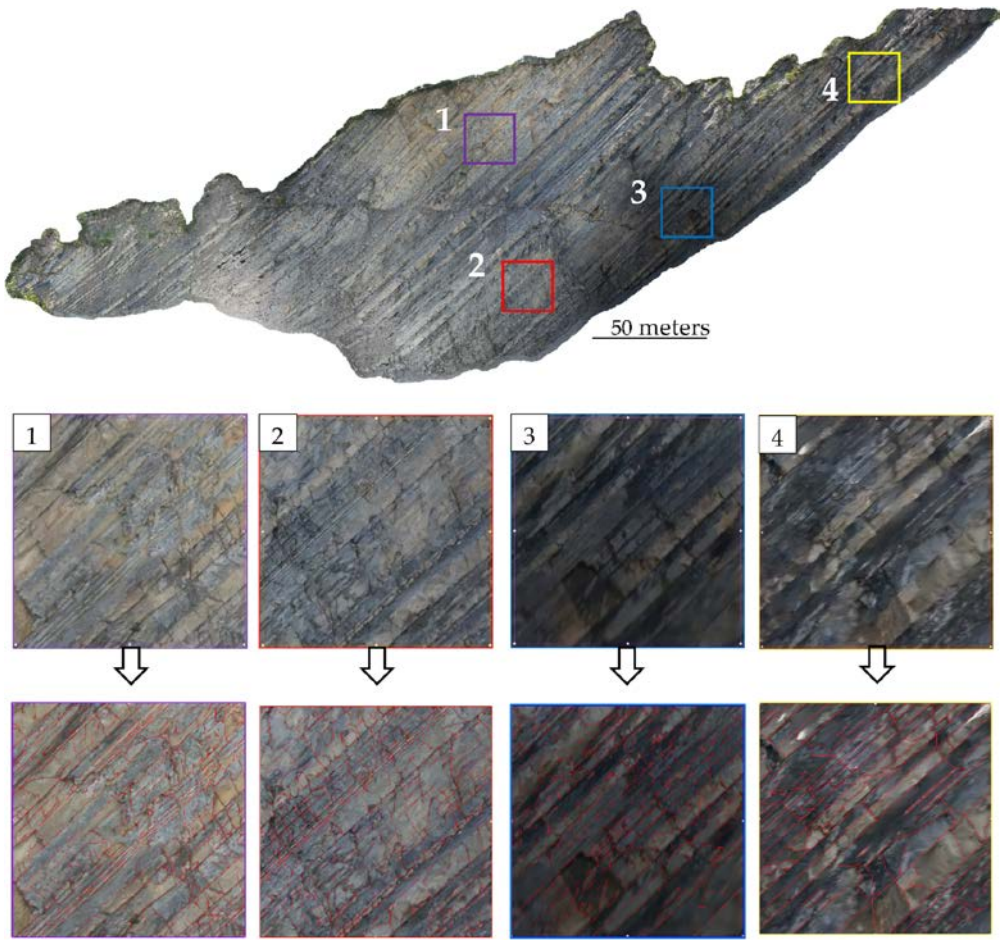

Figure 9. Orthomosaic of the Poggio Baldi rock scarp. 20x20m frames for each source sector (top); Details of source sector frames (1, 2, 3, 4) with the manually traced fractures in red (bottom).

The resulting mean spacing values, gathered from both PC-based spacing distributions and orthophoto interpretation for each joint set and sector, are presented in Table 3. It is clear evidence that the 2D-based discontinuity analysis returns far lower values of mean spacing for J2 (i.e., J2-OM in Table 3), which never exceed 1.5 meters. This contrasts with the results of bedding spacings obtained from the 3D fracture analysis that returns mean spacing values up to 7 meters.

After calculating the formed block based on the intersection of J1, J2 and J3, the resulting volumes (Figure 11) were determined for both the PC and the PC integrated with the orthomosaic (PC+OM) joint analysis. The mean volumes of formed blocks obtained from the PC-based spacing correspond to 39.75 m^3, 10.93 m^3, 26.01 m^3, and 14.79 m^3; while the PC+OM-based spacing analysis returns volumes of about 5.17 m^3, 4.76 m^3, 8.65 m^3, and 9.48 m^3 for sectors 1, 2, 3, and 4 respectively (Figure 11).

Preprints (www.preprints.org) | NOT PEER-REVIEWED | Posted: 8 December 2022 doi:10.20944/preprints202212.0142.v1

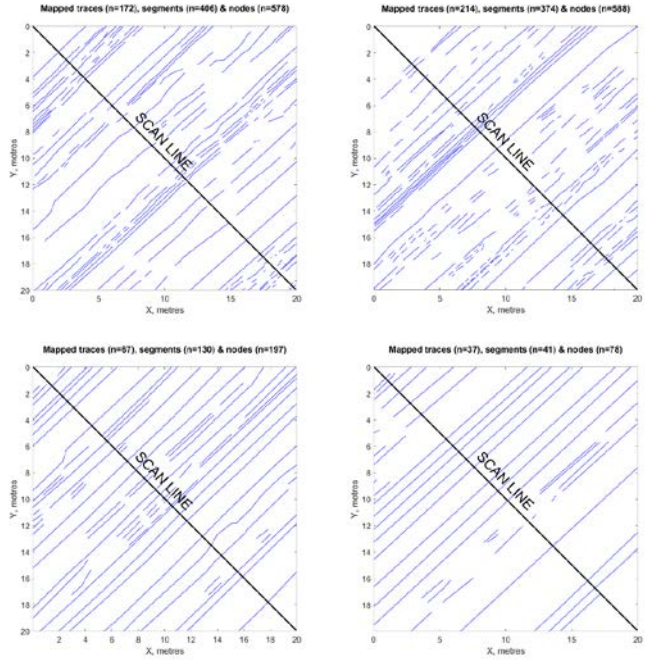

Figure 10. Bedding strata manually traced from the orthomosaic within the box of each source sector.

Table 3. Joint set normal mean spacings in the different source sectors.

Joint Set	Z1	Z2	Z3	Z4
J1	1.902	1.449	1.197	1.443
J2	7.223	2.227	2.767	2.151
J2 - OM	0.940	0.970	0.920	1.380
J3	2.894	3.384	7.858	4.764
J4	1.569	1.536	1.450	1.455
J5	1.458	1.975	1.715	1.146

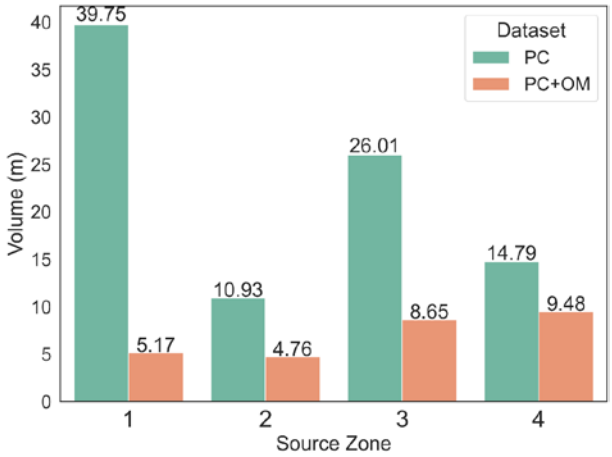

Figure 11. Mean block volume estimation by source sector and dataset.

4.3 3D Rockfall Trajectory Analysis

Two accumulation zone, A and B, were identified (Figure12a); accumulation zone A represents the area where most of the accumulation occur (small volume blocks – Figure 5) while accumulation zone B represent the area where sparse higher volume blocks can

Preprints (www.preprints.org) | NOT PEER-REVIEWED | Posted: 8 December 2022 doi:10.20944/preprints202212.0142.v1

arrive and has been defined integrating M3C2 analysis (Figure 5) and field and orthophoto observations. The accumulation zones and the rockfall fragment inventory were taken into consideration during the calibration phases of the models, offering a clear spatial distribution of the block volumetric classes. Finally, based on GIS interpretation and field survey, a land-use map, with associated rockfall propagation characteristics, was created for use as input for subsequent RF3D (Figura 12c). In Table 4 the parameters used in the formal RF3D simulations are provided.

The rockfall scenarios were hypothesised based on the formed rock block volume estimation, as reported in Figure 11.

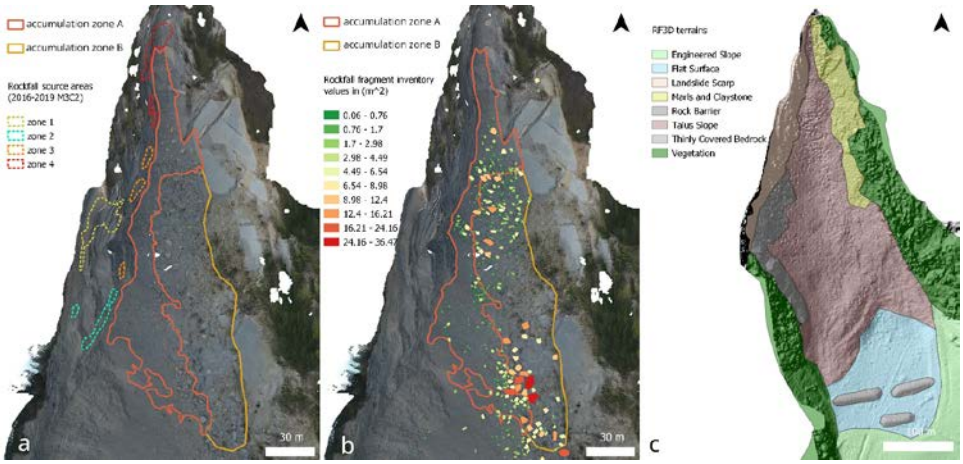

Figure 12. Rockfall accumulation zones in the upper PB landslide. The source areas as reported by the M3C2 analysis are shown in panel a. The terrain subdivisions adopted for the RF3D modelling are reported in panel c.

Table 4. RF3D Parameters.

Terrain description	RF3D Soil type	rg70 [m]	rg20 [m]	rg10 [m]	R_n avg	R_n range
Landslide scarp	6	0	0.1	0.5	0.53	0.48 - 0.58
Thinly covered bedrock	5	0.1	0.2	0.3	0.43	0.39 - 0.47
Marls and claystones	3	0	0.1	0.3	0.33	0.30 - 0.36
Talus slope	3	0.25	0.5	0.9	0.33	0.30 - 0.36
Flat surface	3	0	0.1	0.5	0.33	0.30 - 0.36
Engineered slope	2	0	0.1	0.2	0.28	0.25 - 0.31
Vegetation	1	0.3	0.4	0.6	0.23	0.21 - 0.25
Rock barrier	1	0	0	100	0.23	0.21 - 0.25

In Figure 13 we report the spatial distribution of the intensity of deposited block, i.e., number of blocks deposited. The NBD layer (Number of Blocks Deposited) is compared against the target areas, where the warm colours represent the highest number of individual blocks that stopped in the pixel. In Table 5 the total number of source cells per Z are reported, given 10000 simulated blocks per cell (i.e., the total number of rock blocks falling from each source area). According to the extensive research carried out by [52,56], the probabilistic models with the lowest and least frequent trajectories (outliers) were removed from the final results, any value below the 1.5% threshold was considered unrealistic under the working assumptions of this simulation. Both NBD layers demonstrate

Preprints (www.preprints.org) | NOT PEER-REVIEWED | Posted: 8 December 2022 doi:10.20944/preprints202212.0142.v1

how the runout of the simulated blocks is distributed well within the M3C2 2016-2019 boundaries; the highest concentration of trajectories end points occur at the very top of the scarp, in the northern most sector, being constrained by the narrow channel, while on the lower portion of the slope the geometry allows for longer horizontal travel distance. The general direction of the rockfall propagation is South-South-East. The rockfall simulation carried out with volumes extracted from PC analysis shows that rock blocks reach the homogeneous scree of the M3C2 extracted accumulation zone A, and overflows on the accumulation area B (Figure 13b). The simulation undertaken using PC+OM dataset seems to better replicate the target defined by the M3C2 extracted accumulation zone A and B with a good cover of accumulation zone A and few blocks reaching zone B (Figure 13a, in agreement with what is highlighted in Figure 5 and 12b).

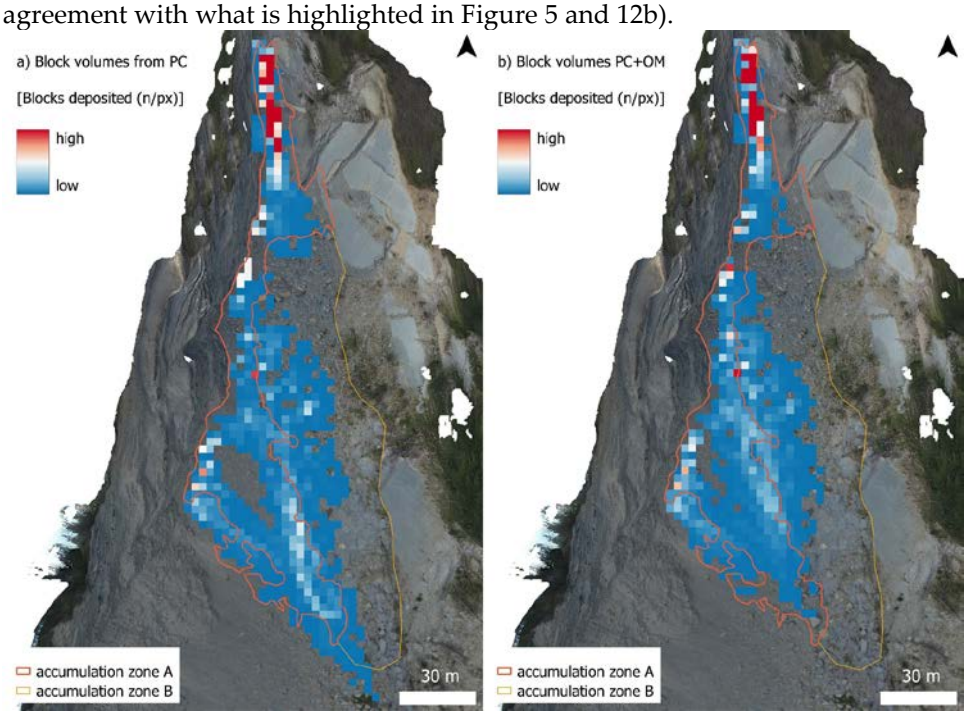

Figure 13. RF3D results. Number of blocks deposited per pixel. Panel a) shows the simulation results obtained with the volume distribution of the PC analysis, while panel b) shows the results from the PC+OM analysis. Refer to table 5 for the simulations' parameters.

Table 5. Simulation characteristics for each source area. 10000 trajectories simulated per source pixel.

Sector	Source pixels	Total trajectories	PC+OM block volume [m³]	PC block volume [m³]
1	48	48 x 10^4	5.17	39.75
2	22	22 x 10^4	4.76	10.93
3	15	15 x 10^4	8.65	26.01
4	84	84 x 10^4	9.48	14.79

5. Discussion

The three-dimensional change detection was carried out between two photogrammetric georeferenced point clouds. The time span is about three years, from April 2016 to May 2019. From this multi-temporal analysis, four active sectors of the rock scarp and a delimited accumulation area were identified, thus providing clear evidence of the state of activity of the landslide. As regards the accumulation area, rock falls tend to accrue along a channel developed at the edges of a residual debris pile related to the March 2010 main reactivation, which is currently slowly moving downslope [25]. This morphology is revealed by vertical profiles shown in Figure 14. Furthermore, the 3D change detection provides an estimate of the involved volumes which represent a proxy for the activity rate.

 doi:10.20944/preprints202212.0142.v1

Lost volumes within the four analysed sectors located over the rock scarp represent most of the total gained volume at the toe, thus revealing the main contribution of these areas in terms of rock block release. This agrees with the findings reported by [24].

As a result, further analysis was performed to investigate the potential block volume involved. For this purpose, information about geometric parameters such as discontinuity sets and joint spacing have been computed by integrating 2D and 3D UAV-derived remote sensing data. We stress that in the case of complex and heterogeneous lithologies, semi-automatic software need to be integrated with expert-controlled tools to obtain accurate results [57]. Based on the 3D point cloud, five different joint sets and their spacing values were identified along the slope. For each studied sector, specific spacing values were derived from the 3D point cloud. However, due to the lack of daylighting bedding strata, its automatic extracted spacing values appears to be unrepresentative for the overall rock mass and the relative block volume overestimated. This is confirmed by the orthomosaic-based analysis, which revealed the true mean spacing value of the bedding within the investigated areas, significantly lower than the value derived with the automatic discontinuity extraction from the 3D point cloud. Hence, the potential formed block volumes computed by integrating both automatic and orthomosaic-based analysis spacing values appear to be more consistent with the in-situ rock blocks (Figure 15), which stand around 5.75 m^3. The performed geo-structural characterization highlighted how different members of the FMA, which correspond to different content ratios of marly and arenaceous strata, result in different formed blocks along the slope. With this perspective, we stress the importance of performing sector-specific study when heterogeneous rock masses must be characterized.

With regards to the rock fall simulation, the PC+OM dataset volume distribution successfully adheres to the available ground truth data, exhibiting a total runout compliant with the accumulation zones A and B. The PC volume distribution has shown good results in relation to accumulation zone A, but an overflow on the accumulation zone B. This is related to the volume of the blocks, overestimated when using automatic spacing extraction. The residual debris highlighted in Figure 14, vertical section A-A', a mound of large rock fragments mixed with loose sediment, is an obstacle for the eastward propagation of the rockfalls, highlighted both by the M3C2 analysis and the RF3D results in Figure 13, and only a sparse number of higher volume blocks reach such area (accumulation zone B).

The use of discrete source areas rather than a diffused hazard modelling offered higher control over the calibration of the model as shown in Figure 15. Individual block detail provided more rigorous comparison between RF3D results and the rockfall fragment inventory and the M3C2 target area. The rockfall hazard practitioners will understand the inherent challenges of defining the range of the MOH values. In this study we failed to find a suitable programmatic approach to characterise the obstacles on the slope and had to rely on manual measurements of the scree slope in the point clouds. The time-independent rockfall hazard analysis explores the effect of geomorphological processes affecting the main scarp and the whole landslide; the RF3D simulation results explore the behaviour of the rockfall activity, especially considering the constraints given by the source and accumulation areas highlighted by the M3C2. This provides a starting point for any further investigation regarding the magnitude-frequency relationship [58] of the Poggio Baldi rockfall activity and future investigation in a similar case study characterized by complex geological-lithological settings.

Preprints (www.preprints.org) | NOT PEER-REVIEWED | Posted: 8 December 2022 doi:10.20944/preprints202212.0142.v1

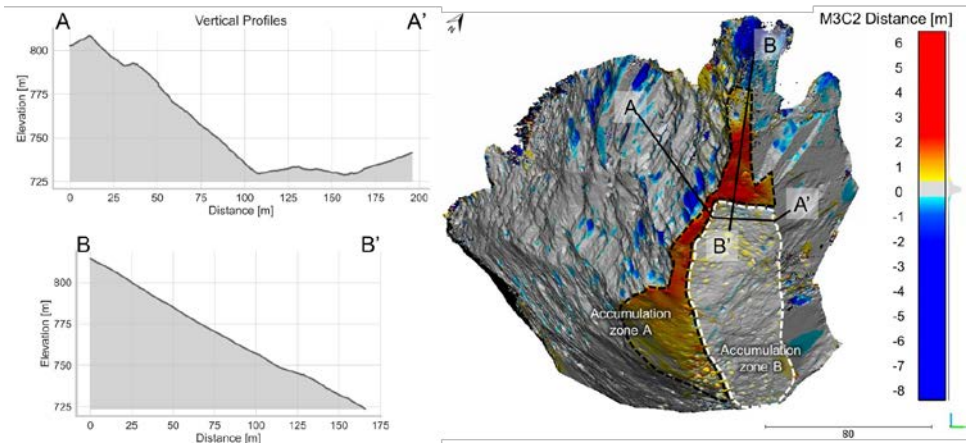

Figure 14. Three-dimensional change detection of UAV-based point clouds with highlighted the accumulation zones A and B (right side). Orthogonal vertical profiles showing the morphology of the slope (left side).

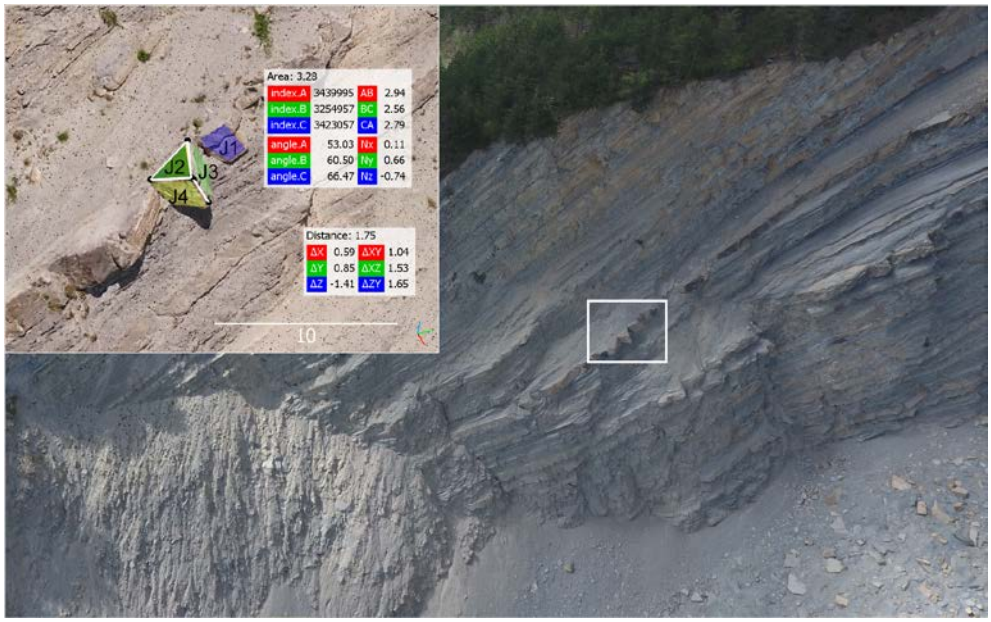

Figure 15. Overview of the left part of the Poggio Baldi landslide rock scarp and details of a typical in-situ rock block dimensions measured from the point cloud (white box).

6. Conclusion

Digital twin models of the Poggio Baldi scarp area have been successfully utilized to provide key data for the monitoring and assessment of rock falls. By combining information derived from three-dimensional point clouds and from the high-resolution orthomosaic it was possible to extract and quantify fracture patterns that characterize the rock mass and define block volumes. Multitemporal surveys allowed us to identify specific sectors of the slope where rockfalls occurs most frequently, as well as the related accumulation zones at its toe. In addition, the overall lost and gained volumes were calculated to assess the activity of the slope.

With the aim of modelling the associated rockfall hazard, we estimated the potential formed block volumes in each active sector of the slope by means of joint spacing values resulting from the integration of 3D automatic extraction tools and 2D discontinuities manual extraction performed from point cloud and orthomosaic data, respectively. The use of both methods was required to provide more representative data due to the unreliable results gathered for bedding strata spacing in the automatic extraction procedure (not enough bedding daylighting surfaces were captured by the PC analysis), thus

highlighting the need of expert judgement when using automatic tools for discontinuity sets extraction. Subsequently, the potential formed blocks were used as input data for the run-out modelling, which was validated based on the 3D change detection results.

The resulting rockfall conceptual model was tested by means of 3D process-based probabilistic trajectory analysis; the parametrization of the model was informed by the geostructural analysis and the available remote sensing datasets and geomorphological observations. A time-independent rockfall hazard assessment demonstrated: i) the geometrical characteristics of the rockfalls affecting the different sectors of the main scarp, ii) the benefits of differentiating the source areas based on 3D change detection, and iii) the importance of using structural derived data for more accurate modeling. Furthermore, the rockfall modeling coupled with the 3D change detection provides further insight into the actual time-dependent behavior of the active processes on the Poggio Baldi slope. In a more general perspective, we demonstrated that the availability of multi-temporal data (3D models or images) of rock-scarps may allow to better calibrate simulations and, consequently, to provide a better design of protection measures. Considering the drastically increased accessibility of tools for multi-temporal data collection we conclude that the systematic collection of Digital Twins of rock-slopes may significantly support rockfall hazard practice.

Supplementary Materials: The following supporting information can be downloaded at: www.mdpi.com/xxx/s1, Figure S1: title; Table S1: title; Video S1: title.

Author Contributions: Conceptualization, C.R., G.M., and M.F.; methodology, C.R., G.M.; formal analysis, C.R. and G.M.; investigation, C.R., G.M, M.F. and P.M.; data curation, C.R. and G.M.; writing—original draft preparation, C.R., G.M.; writing—review and editing, M.F., M.E., J.C., and P.M.; supervision, P.M. All authors have read and agreed to the published version of the manuscript.

Funding: This research is framed in the project "Dipartimento di Eccellenza per le Scienze della Terra—Laboratorio naturale di Poggio Baldi" (Sapienza University of Rome—Years 2018–2022, P.I. Prof. Paolo Mazzanti). This work was also supported by NHAZCA Srl, spin-off company of the University of Rome "Sapienza", the Department of Earth Sciences of the University of Rome "Sapienza", and the Parco Nazionale delle Foreste Casentinesi, Monte Falterona e Campigna.

Data Availability Statement: Data is contained within the article or supplementary material.

Acknowledgments: The authors wish to thank the Pro loco Corniolo-Campigna Association and G. Pini for the logistic support provided during the field surveys.

Conflicts of Interest: The authors declare no conflict of interest.

References

1. Francioni, M.; Antonaci, F.; Sciarra, N.; Robiati, C.; Coggan, J.; Stead, D.; Calamita, F. Application of Unmanned Aerial Vehicle Data and Discrete Fracture Network Models for Improved Rockfall Simulations. *Remote Sensing* **2020**, *12*, 2053, doi:10.3390/rs12122053.
2. Sarro, R.; Riquelme, A.; García-Davalillo, J.C.; Mateos, R.M.; Tomás, R.; Pastor, J.L.; Cano, M.; Herrera, G. Rockfall Simulation Based on UAV Photogrammetry Data Obtained during an Emergency Declaration: Application at a Cultural Heritage Site. *Remote Sensing* **2018**, *10*, 1923, doi:10.3390/rs10121923.
3. Bonneau, D.A.; DiFrancesco, P.-M.; Hutchinson, D.J. A Method for Vegetation Extraction in Mountainous Terrain for Rockfall Simulation. *Remote Sensing of Environment* **2020**, *251*, 112098, doi:10.1016/j.rse.2020.112098.
4. Rossi, M.; Sarro, R.; Reichenbach, P.; Mateos, R.M. Probabilistic Identification of Rockfall Source Areas at Regional Scale in El Hierro (Canary Islands, Spain). *Geomorphology* **2021**, *381*, 107661, doi:10.1016/j.geomorph.2021.107661.
5. Guzzetti, F.; Reichenbach, P.; Ghigi, S. Rockfall Hazard and Risk Assessment Along a Transportation Corridor in the Nera Valley, Central Italy. *Environmental Management* **2004**, *34*, 191–208, doi:10.1007/s00267-003-0021-6.

6. Michoud, C.; Derron, M.-H.; Horton, P.; Jaboyedoff, M.; Baillifard, F.-J.; Loye, A.; Nicolet, P.; Pedrazzini, A.; Queyrel, A. Rockfall Hazard and Risk Assessments along Roads at a Regional Scale: Example in Swiss Alps. *Natural Hazards and Earth System Sciences* **2012**, *12*, 615–629, doi:10.5194/nhess-12-615-2012.
7. Scavia, C.; Barbero, M.; Castelli, M.; Marchelli, M.; Peila, D.; Torsello, G.; Vallero, G. Evaluating Rockfall Risk: Some Critical Aspects. *Geosciences* **2020**, *10*, 98, doi:10.3390/geosciences10030098.
8. Gili, J.A.; Ruiz-Carulla, R.; Matas, G.; Moya, J.; Prades, A.; Corominas, J.; Lantada, N.; Núñez-Andrés, M.A.; Buill, F.; Puig, C.; et al. Rockfalls: Analysis of the Block Fragmentation through Field Experiments. *Landslides* **2022**, *19*, 1009–1029, doi:10.1007/s10346-021-01837-9.
9. Gallo, I.G.; Martínez-Corbella, M.; Sarro, R.; Iovine, G.; López-Vinielles, J.; Hérnandez, M.; Robustelli, G.; Mateos, R.M.; García-Davalillo, J.C. An Integration of UAV-Based Photogrammetry and 3D Modelling for Rockfall Hazard Assessment: The Cárcavos Case in 2018 (Spain). *Remote Sensing* **2021**, *13*, 3450, doi:10.3390/rs13173450.
10. Robiati, C.; Eyre, M.; Vanneschi, C.; Francioni, M.; Venn, A.; Coggan, J. Application of Remote Sensing Data for Evaluation of Rockfall Potential within a Quarry Slope. *ISPRS International Journal of Geo-Information* **2019**, *8*, 367, doi:10.3390/ijgi8090367.
11. Bonneau, D.; DiFrancesco, P.-M.; Hutchinson, D.J. Surface Reconstruction for Three-Dimensional Rockfall Volumetric Analysis. *ISPRS International Journal of Geo-Information* **2019**, *8*, 548, doi:10.3390/ijgi8120548.
12. Sarro, R.; María Mateos, R.; Reichenbach, P.; Aguilera, H.; Riquelme, A.; Hernández-Gutiérrez, L.E.; Martín, A.; Barra, A.; Solari, L.; Monserrat, O.; et al. Geotechnics for Rockfall Assessment in the Volcanic Island of Gran Canaria (Canary Islands, Spain). *Journal of Maps* **2020**, *16*, 605–613, doi:10.1080/17445647.2020.1806125.
13. Francioni, M.; Stead, D.; Sciarra, N.; Calamita, F. A New Approach for Defining Slope Mass Rating in Heterogeneous Sedimentary Rocks Using a Combined Remote Sensing GIS Approach. *Bull Eng Geol Environ* **2019**, *78*, 4253–4274, doi:10.1007/s10064-018-1396-1.
14. McKenzie, D. Active Tectonics of the Mediterranean Region. *Geophysical Journal International* **1972**, *30*, 109–185, doi:10.1111/j.1365-246X.1972.tb02351.x.
15. Martelli, L.; Camassi, R.; Catanzariti, R.; Fornaciari, L.; Spadafora, E. Explanatory Notes of the Geological Map of Italy, Scale 1:50,000, Sheet 265 "Bagno Di Romagna." **2002**.
16. Ricci Lucchi, F. The Miocene Marnoso-Arenacea Turbidites, Romagna and Umbria Apennines. Excursion N 7, Excursion Guidebook. In Proceedings of the 2nd European Regional Meeting IAS; 1981.
17. Benini, A.; Farabegoli, E.; Martelli, L.; Severi, P. Stratigrafia e Paleogeografia Del Gruppo Di S. Sofia (Alto Appennino Forlivese). *Memorie descrittive della Carta Geologica d?italia* **1992**, *46*, 231–243.
18. Mutti, E.; Bernoulli, D.; Lucchi, F.R.; Tinterri, R. Turbidites and Turbidity Currents from Alpine 'Flysch' to the Exploration of Continental Margins. *Sedimentology* **2009**, *56*, 267–318, doi:https://doi.org/10.1111/j.1365-3091.2008.01019.x.
19. Esposito, C.; Di Luzio, E.; Baleani, M.; Troiani, F.; Seta, M.D.; Bozzano, F.; Mazzanti, P. FOLD ARCHITECTURE PREDISPOSING DEEP-SEATED GRAVITATIONAL SLOPE DEFORMATIONS WITHIN A FLYSCH SEQUENCE IN THE NORTHERN APENNINES (ITALY). *Geomorphology* **2021**, 107629, doi:10.1016/j.geomorph.2021.107629.
20. Bortolotti, V. Guide Geologiche Regionali. *Appennino Tosco-emiliano. BE-MA, Milano* **1992**.
21. Benini, A.; Biavati, G.; Generali, M.; Pizziolo, M. The Poggio Baldi Landslide (High Bidente Valley): Event and Post-Event Analysis and Geological Characterization. *Proceedings 7th EUREGEO, Bologna, Italy* **2012**, *1*.
22. Mazzanti, P.; Bozzano, F.; Brunetti, A.; Caporossi, P.; Esposito, C.; Mugnozza, G.S. Experimental Landslide Monitoring Site of Poggio Baldi Landslide (Santa Sofia, N-Apennine, Italy). In Proceedings of the Advancing Culture of Living with Landslides; Mikoš, M., Arbanas, Ž., Yin, Y., Sassa, K., Eds.; Springer International Publishing: Cham, 2017; pp. 259–266.

23. Varnes, D.J. Slope Movement Types and Processes. *Special report* **1978**, *176*, 11–33.
24. Mazzanti, P.; Caporossi, P.; Brunetti, A.; Mohammadi, F.I.; Bozzano, F. Short-Term Geomorphological Evolution of the Poggio Baldi Landslide Upper Scarp via 3D Change Detection. *Landslides* **2021**.
25. Romeo, S.; Cosentino, A.; Giani, F.; Mastrantoni, G.; Mazzanti, P. Combining Ground Based Remote Sensing Tools for Rockfalls Assessment and Monitoring: The Poggio Baldi Landslide Natural Laboratory. *Sensors* **2021**, *21*, 2632, doi:10.3390/s21082632.
26. Girardeau-Montaut, D. Détection de Changement Sur Des Données Géométriques Tridimensionnelles. phdthesis, Télécom ParisTech, 2006.
27. Spetsakis, M.E.; Aloimonos, J. (Yiannis) Structure from Motion Using Line Correspondences. *Int J Comput Vision* **1990**, *4*, 171–183, doi:10.1007/BF00054994.
28. Boufama, B.; Mohr, R.; Veillon, F. Euclidean Constraints for Uncalibrated Reconstruction. In Proceedings of the 1993 (4th) International Conference on Computer Vision; May 1993; pp. 466–470.
29. Szeliski, R.; Kang, S.B. Recovering 3D Shape and Motion from Image Streams Using Nonlinear Least Squares. *Journal of Visual Communication and Image Representation* **1994**, *5*, 10–28, doi:10.1006/jvci.1994.1002.
30. Seitz, S.M.; Curless, B.; Diebel, J.; Scharstein, D.; Szeliski, R. A Comparison and Evaluation of Multi-View Stereo Reconstruction Algorithms. In Proceedings of the 2006 IEEE Computer Society Conference on Computer Vision and Pattern Recognition (CVPR'06); June 2006; Vol. 1, pp. 519–528.
31. James, M.R.; Robson, S. Straightforward Reconstruction of 3D Surfaces and Topography with a Camera: Accuracy and Geoscience Application. *Journal of Geophysical Research: Earth Surface* **2012**, *117*, doi:10.1029/2011JF002289.
32. Luhmann, T.; Robson, S.; Kyle, S.; Boehm, J. *Close-Range Photogrammetry and 3D Imaging*; De Gruyter, 2019; ISBN 978-3-11-060725-3.
33. Carrivick, J.L.; Smith, M.W.; Quincey, D.J. *Structure from Motion in the Geosciences*; John Wiley & Sons, 2016; ISBN 978-1-118-89583-2.
34. Snavely, N.; Seitz, S.M.; Szeliski, R. Modeling the World from Internet Photo Collections. *Int J Comput Vis* **2008**, *80*, 189–210, doi:10.1007/s11263-007-0107-3.
35. Arya, S.; Mount, D.M.; Netanyahu, N.S.; Silverman, R.; Wu, A.Y. An Optimal Algorithm for Approximate Nearest Neighbor Searching Fixed Dimensions. *J. ACM* **1998**, *45*, 891–923, doi:10.1145/293347.293348.
36. Fischler, M.A.; Bolles, R.C. Random Sample Consensus: A Paradigm for Model Fitting with Applications to Image Analysis and Automated Cartography. *Commun. ACM* **1981**, *24*, 381–395, doi:10.1145/358669.358692.
37. Lague, D.; Brodu, N.; Leroux, J. Accurate 3D Comparison of Complex Topography with Terrestrial Laser Scanner: Application to the Rangitikei Canyon (N-Z). *ISPRS Journal of Photogrammetry and Remote Sensing* **2013**, *82*, 10–26, doi:10.1016/j.isprsjprs.2013.04.009.
38. Stumpf, A.; Malet, J.-P.; Allemand, P.; Pierrot-Deseilligny, M.; Skupinski, G. Ground-Based Multi-View Photogrammetry for the Monitoring of Landslide Deformation and Erosion. *Geomorphology* **2015**, *231*, 130–145, doi:10.1016/j.geomorph.2014.10.039.
39. Riquelme, A.J.; Abellán, A.; Tomás, R.; Jaboyedoff, M. A New Approach for Semi-Automatic Rock Mass Joints Recognition from 3D Point Clouds. *Computers & Geosciences* **2014**, *68*, 38–52, doi:10.1016/j.cageo.2014.03.014.
40. Riquelme, A.; Cano, M.; Tomás, R.; Abellán, A. Identification of Rock Slope Discontinuity Sets from Laser Scanner and Photogrammetric Point Clouds: A Comparative Analysis. *Procedia Engineering* **2017**, *191*, 838–845, doi:10.1016/j.proeng.2017.05.251.
41. Friedman, J.H. A Recursive Partitioning Decision Rule for Nonparametric Classification. *IEEE Transactions on Computers* **1977**, *26*, 404–408, doi:10.1109/TC.1977.1674849.

42. Botev, Z.I.; Grotowski, J.F.; Kroese, D.P. Kernel Density Estimation via Diffusion. *The Annals of Statistics* **2010**, *38*, 2916–2957, doi:10.1214/10-AOS799.
43. Ester, M.; Kriegel, H.-P.; Sander, J.; Xu, X. A Density-Based Algorithm for Discovering Clusters in Large Spatial Databases with Noise. In Proceedings of the Proceedings of the Second International Conference on Knowledge Discovery and Data Mining; AAAI Press: Portland, Oregon, Agosto 1996; pp. 226–231.
44. Farmakis, I.; Hutchinson, D.J. Semi-Automated Discontinuity Orientation Extraction in Complex Rock Masses Using Single-Scan LiDAR Data. In Proceedings of the Geophysical Research Abstracts; 2019; Vol. 21.
45. Riquelme, A.J.; Abellán, A.; Tomás, R. Discontinuity Spacing Analysis in Rock Masses Using 3D Point Clouds. *Engineering Geology* **2015**, *195*, 185–195, doi:10.1016/j.enggeo.2015.06.009.
46. Palmstrom, A. Measurements of and Correlations between Block Size and Rock Quality Designation (RQD). *Tunnelling and Underground Space Technology* **2005**, *20*, 362–377, doi:10.1016/j.tust.2005.01.005.
47. Healy, D.; Rizzo, R.E.; Cornwell, D.G.; Farrell, N.J.C.; Watkins, H.; Timms, N.E.; Gomez-Rivas, E.; Smith, M. FracPaQ: A MATLAB™ Toolbox for the Quantification of Fracture Patterns. *Journal of Structural Geology* **2017**, *95*, 1–16, doi:10.1016/j.jsg.2016.12.003.
48. Ferrari, F.; Giacomini, A.; Thoeni, K. Qualitative Rockfall Hazard Assessment: A Comprehensive Review of Current Practices. *Rock Mech Rock Eng* **2016**, *49*, 2865–2922, doi:10.1007/s00603-016-0918-z.
49. Volkwein, A.; Schellenberg, K.; Labiouse, V.; Agliardi, F.; Berger, F.; Bourrier, F.; Dorren, L.K.A.; Gerber, W.; Jaboyedoff, M. Rockfall Characterisation and Structural Protection – a Review. *Natural Hazards and Earth System Sciences* **2011**, *11*, 2617–2651, doi:10.5194/nhess-11-2617-2011.
50. Hantz, D.; Corominas, J.; Crosta, G.B.; Jaboyedoff, M. Definitions and Concepts for Quantitative Rockfall Hazard and Risk Analysis. *Geosciences* **2021**, *11*, 158, doi:10.3390/geosciences11040158.
51. Noël, F.; Cloutier, C.; Jaboyedoff, M.; Locat, J. Impact-Detection Algorithm That Uses Point Clouds as Topographic Inputs for 3D Rockfall Simulations. *Geosciences* **2021**, *11*, 188, doi:10.3390/geosciences11050188.
52. Dorren, L.K.A. A Review of Rockfall Mechanics and Modelling Approaches. *Progress in Physical Geography: Earth and Environment* **2003**, *27*, 69–87, doi:10.1191/0309133303pp359ra.
53. Ritchie, A.M. EVALUATION OF ROCKFALL AND ITS CONTROL. *Highway Research Record* **1963**.
54. Mitchell, A.; Hungr, O. Theory and Calibration of the Pierre 2 Stochastic Rock Fall Dynamics Simulation Program. *Can. Geotech. J.* **2017**, *54*, 18–30, doi:10.1139/cgj-2016-0039.
55. Asteriou, P.; Tsiambaos, G. Effect of Impact Velocity, Block Mass and Hardness on the Coefficients of Restitution for Rockfall Analysis. *International Journal of Rock Mechanics and Mining Sciences* **2018**, *106*, 41–50, doi:10.1016/j.ijrmms.2018.04.001.
56. Dorren, L.K.A. Rockyfor3D (v5. 2) Revealed–Transparent Description of the Complete 3D Rockfall Model. EcorisQ Paper (Www. Ecorisq. Org): 33 p 2016.
57. Vanneschi, C.; Rindinella, A.; Salvini, R. Hazard Assessment of Rocky Slopes: An Integrated Photogrammetry–GIS Approach Including Fracture Density and Probability of Failure Data. *Remote Sensing* **2022**, *14*, 1438, doi:10.3390/rs14061438.
58. Moos, C.; Bontognali, Z.; Dorren, L.; Jaboyedoff, M.; Hantz, D. Estimating Rockfall and Block Volume Scenarios Based on a Straightforward Rockfall Frequency Model. *Engineering Geology* **2022**, *309*, 106828, doi:10.1016/j.enggeo.2022.106828.